Phonon-coupled ultrafast interlayer charge oscillation at van der Waals heterostructure interfaces

Qijing Zheng,[1] Yu Xie,[2] Zhenggang Lan,[2] Oleg V. Prezhdo,[3] Wissam A. Saidi,[4] and Jin Zhao[1,5,6,*]

[1]*ICQD/Hefei National Laboratory for Physical Sciences at Microscale, and Key Laboratory of Strongly-Coupled Quantum Matter Physics, Chinese Academy of Sciences, and Department of Physics, University of Science and Technology of China, Hefei, Anhui 230026, China*

[2]*Key Laboratory of Biobased Materials, Qingdao Institute of Bioenergy and Bioprocess Technology, Chinese Academy of Sciences, Qingdao, Shandong 266101, China*

[3]*Departments of Chemistry, and Physics and Astronomy, University of Southern California, Los Angeles, California 90089, USA*

[4]*Department of Mechanical Engineering and Materials Science, University of Pittsburgh, Pittsburgh, Pennsylvania 15261, USA*

[5]*Department of Physics and Astronomy, University of Pittsburgh, Pittsburgh, Pennsylvania 15260, USA*

[6]*Synergetic Innovation Center of Quantum Information & Quantum Physics, University of Science and Technology of China, Hefei, Anhui 230026, China*

(Received 8 September 2017; revised manuscript received 16 April 2018; published 14 May 2018)

Van der Waals (vdW) heterostructures of transition-metal dichalcogenide (TMD) semiconductors are central not only for fundamental science, but also for electro- and optical-device technologies where the interfacial charge transfer is a key factor. Ultrafast interfacial charge dynamics has been intensively studied, however, the atomic scale insights into the effects of the electron-phonon (*e-p*) coupling are still lacking. In this paper, using time dependent *ab initio* nonadiabatic molecular dynamics, we study the ultrafast interfacial charge transfer dynamics of two different TMD heterostructures MoS_2/WS_2 and $MoSe_2/WSe_2$, which have similar band structures but different phonon frequencies. We found that $MoSe_2/WSe_2$ has softer phonon modes compared to MoS_2/WS_2, and thus phonon-coupled charge oscillation can be excited with sufficient phonon excitations at room temperature. In contrast, for MoS_2/WS_2, phonon-coupled interlayer charge oscillations are not easily excitable. Our study provides an atomic level understanding on how the phonon excitation and *e-p* coupling affect the interlayer charge transfer dynamics, which is valuable for both the fundamental understanding of ultrafast dynamics at vdW hetero-interfaces and the design of novel quasi-two-dimensional devices for optoelectronic and photovoltaic applications.

DOI: 10.1103/PhysRevB.97.205417

I. INTRODUCTION

Van der Waals (vdW) heterostructures composed of two-dimensional (2D) transition-metal dichalcogenides (TMDs) have optical band gaps in the visible spectral region and strong light-matter interactions [1–7]. This makes them of potential interest to different applications in the fields of electronics, optoelectronics, and energy harvesting [2,3,8–14].

For the applications in solar energy conversion and optoelectronics, efficient charge separation is a key factor, which can be accomplished by fast interlayer charge transfer. Most vertically stacked TMD heterostructures show type II band alignment where the conduction band minimum (CBM) and the valence band maximum (VBM) reside on different layers [15–19]. Such a feature facilitates the electron-hole separation after a photoexcitation, and consequently, increases the photocarrier lifetime. However, fast carrier transport is typically associated with materials with strong chemical bonding rather than with materials that have atomically sharp interfaces and are bound by vdW forces, as in the case of TMD heterostructures. Furthermore, excitons in single-layer TMDs have large binding energies of the order of 0.6–1.0 eV, and their wave functions are localized in two dimensions [4,5,20–22]. These factors are expected to inhibit interlayer charge transfer in the TMDs.

There have been intensive investigations to understand the interlayer charge transfer dynamics in TMD heterostructures recently [9,23–29]. Contrary to common expectations, ultrafast interlayer charge transfer has been experimentally observed in different TMD heterostructures [9,23–25]. For example, Hong *et al.* used resonant femtosecond pump pulse to selectively excite intralayer excitons in MoS_2, and transient absorption to probe the subsequent charge transfer. This study found that the holes quickly transfer to the WS_2 layer due to the type II band alignment, whereas electrons remain in the MoS_2 layer, forming an interlayer exciton. The transient absorption signals from the photoexcited electrons in MoS_2 and holes in WS_2 had a rise time within 50 fs. In other transient absorption measurements on $MoS_2/MoSe_2$, Ceballos *et al.* also found an instrument limited time scale of less than 200 fs for both the hole and electron transfer [23]. Moreover, Zhu *et al.* reported an efficient quenching of photoluminescence from intralayer exciton to interlayer exciton by the interlayer charge transfer when a MoS_2/WSe_2 heterojunction is formed [24].

It is essential to understand the unexpected ultrafast interfacial charge transfer at atomic scale. As already shown in some of the investigations on ultrafast carrier dynamics in TMD systems [28,30], the dynamics of electrons are naturally coupled to the motion of nuclei, namely, the phonons. The development of time-dependent nonadiabatic molecular

*zhaojin@ustc.edu.cn

dynamics (NAMD) makes it possible to investigate the excited carrier dynamics and their coupling to phonons using state-of-the-art *ab initio* calculations [31]. Combining time-dependent DFT (TDDFT) with fewest switches surface hopping (FSSH) scheme, the excited carrier dynamics have been investigated in different condensed matter systems [32–35]. We have used this method to investigate the time-dependent excited carrier dynamics at various surfaces and interfaces [28,36,37]. In our recent work, the phonon-assisted ultrafast excited hole transfer at MoS_2/WS_2 is revealed [28]. In order to systematically understand how the electron-phonon (*e-p*) coupling affect the ultrafast carrier dynamics at TMD interface, we use *ab initio* nonadiabatic molecular dynamics (NAMD) to investigate the excited interfacial electron transfer at two different TMD heterostructures MoS_2/WS_2 and $MoSe_2/WSe_2$. These two different TMD heterostructures have similar band structures but different phonon frequencies. It is found that for both of them, the electron transfer is mostly coupled with the A_1 intralayer optical phonon mode. By replacing S with Se, A_1 phonon mode is soften in $MoSe_2/WSe_2$ and therefore more phonons can be easily excited at room temperature. Such sufficient phonon excitation can drive electron oscillation between $MoSe_2/WSe_2$. When temperature is reduced from room temperature to 100 K, such charge oscillation is suppressed along with the phonon frozen. In contrast, in MoS_2/WS_2, the phonons have relatively high frequencies that are not easily excited at room temperature. Therefore, the phonon-coupled electron oscillation is not observed. The atomic level insights into how the exciton binding and *e-p* coupling affect the carrier dynamics at vdW TMD heterostructure interface is not only valuable for the fundamental understanding of the ultrafast interface charge transfer, but also provide a new strategy for the design of novel quasi-2D devices for optoelectronic and photovoltaic applications.

II. METHODOLOGY

The *ab initio* NAMD simulations are carried out using homemade code HEFEI-NAMD [38], which augments the Vienna *ab initio* simulation package (VASP) [39–42] with the NAMD capabilities within TDDFT and FSSH similar to Refs. [32,43,44]. This approach is computationally tractable and has been utilized in several studies of the relaxation progress of photogenerated carriers in semiconducting materials [33,36]. The electron-nuclear interactions are described using projector augmented wave (PAW) method [45]. We use the Perdew-Burke-Ernzerhof (PBE) exchange-correlation functional in all calculations [46]. VdW interactions are included in the simulations using the D2 approach [47]. The TMD heterostructures are modeled using an orthogonal 3×3 supercell with 108 atoms with Brillouin zone (BZ) sampled at the Γ point. The optimized lattice constants of MoS_2 and WS_2 monolayer are identical to the third number after the decimal point, i.e., 3.185 Å. For $MoSe_2$ and WSe_2, the optimized lattice constants are 3.320 and 3.318 Å, respectively. We use the lattice constants of 3.185 and 3.320 Å for MoS_2/WS_2 and $MoSe_2/WSe_2$. Seven irreducible K points including the Γ and K points of the primitive cell BZ are included and can be assigned by unfolding the energy bands [48]. The electronic structure is calculated using the optimized geometry at 0 K. After the geometry optimization, we use velocity rescaling to bring the temperature of the system to either 300 or 100 K; a 5 ps microcanonical *ab initio* molecular dynamics trajectory is then generated with a time step of 1 fs. The NAMD results are obtained by averaging over 100 different initial configurations chosen randomly from the first 3 ps of the molecular dynamics trajectory. For each chosen structure, we sample 2×10^4 NAMD trajectories 2 ps in length.

The extent of charge transfer from one TMD layer to another is computed by integrating the photoexcited carrier density over the region of the simulated cell occupied by one of the TMD layer, e.g., WS_2,

$$\int \rho(r,t)dr = \int |\psi(r,t)|^2 dr = \sum_{i,j} c_i^*(t)c_j(t) \int \varphi_i^*[r,R(t)]\varphi_j[r,R(t)]dr, \quad (1)$$

where ρ is the photoexcited charge density, ψ is the total wave function, which can be expanded into the Kohn-Sham wave functions φ_i and φ_j with c_i and c_j as the coefficients. The coefficients represent the occupation of excited carriers on Kohn-Sham orbitals. Taking the time derivative of Eq. (1) gives the expression for adiabatic (AD) and nonadiabatic (NA) contribution to charge transfer:

$$\frac{d\int \rho(r,t)dr}{dt} = \sum_{ij} \left\{ \frac{d(c_i^* c_j)}{dt} \int \varphi_i^* \varphi_j dr + c_i^* c_j \frac{d\int \varphi_i^* \varphi_j dr}{dt} \right\}. \quad (2)$$

The change in the charge density described by the first term on the right-hand side of Eq. (2) is due to change of state occupation of the adiabatic KS states, which we refer to as the nonadiabatic transition term. The second term describes effects due to changes of localization of the KS adiabatic state, hence the name adiabatic transfer. The contribution to the total charge transfer is obtained by further integrating the two terms on the right-hand side of Eq. (2). More details of the calculation methods can be found in the Supplemental Material [39,42–44,46,48–50]. The discussion of spin orbital coupling effects, stacking effects, K-grid effects, and different functional effects are also included in the Supplemental Material [5,19,48,51–55].

III. RESULTS AND DISCUSSION

A. Electronic structure

We choose the most stable C7 stacking to investigate [19]. Before describing the NAMD results, we first inspect the electronic band structures of the MoS_2/WS_2 and $MoSe_2/WSe_2$ using the primitive cell with $(11 \times 11 \times 1)$ K points as shown in Figs. 1(a)–1(b). As can be seen, the band structures of these two heterostructures show significant similarities. Both of them have type II band alignment. Valence band maximum (VBM) and conduction band minimum (CBM) are located on WX_2 (X = S, Se) @Γ and MoX_2@K respectively. As indicted by the color strip in Fig. 1 and the corresponding orbital distributions, the orbital hybridization varies with the momentum within a band. For conduction bands (CBs) at the K point, the interlayer hybridization is weak because the dominant

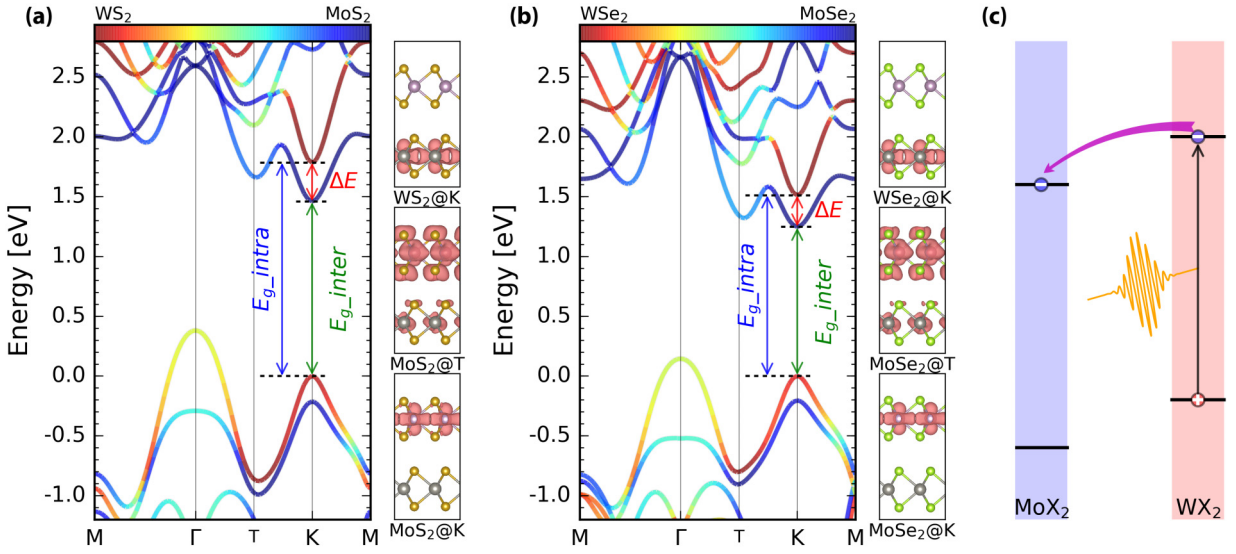

FIG. 1. Band structures and orbital spatial distributions of (a) MoS_2/WS_2 and (b) $MoSe_2/WSe_2$ heterostructures. The energy of WX_2@K_VB is set to zero. The color strip indicates the localization of the states. The photoexcitation and the initial electron/hole distribution is indicated in (a)–(b). The schematic of electron transfer in TMD heterostructure is shown in (c).

metal d_{xy} and $d_{x^2-y^2}$ and S (Se) p_x and p_y orbitals are mostly localized within the TMD layer. There is another local energy minimum in the CB of MoX_2, which is located midway along the T path between Γ and K (noted as MX_2@T). The interlayer hybridization at this point is relatively stronger. In this report we focus on the electron dynamics schematically shown in Fig. 1(c). The intralayer exciton is first excited at WX_2@K, and subsequently the excited electron transfers to MoX_2. In the latter process, the scattering with phonon is required. Recent experimental measurements proved that the interlayer exciton formation in MoX_2/WX_2 with both electron and hole localized at K/K' points in momentum space [56–59]. Therefore in this investigation we consider the excited hole remains at K point in the valance band of WX_2(WX_2@K_VB), and the intralayer exciton converts into an interlayer exciton after the electron transfer. The electron transfer route can be through WX_2@K directly to MoX_2@K. It can also transfer from WX_2@K first to MoX_2@T, and then relax to MoX_2@K, which is the CBM. In all the investigations we take the energy of WX_2@K_VB, where the excited hole is located, as the energy reference.

B. Thermal fluctuations of the CB states

We focus on the electronic states that are involved in the dynamics near CBM considering that we are investigating the electron transfer at TMD heterostructure interface. The energy evolution of the states near CBM for MoX_2/WX_2 at 300 and 100 K are shown in Figs. 2(a)–2(d). Here we use the same color map as in Fig. 1 to show the orbitals localization. Because we are using an orthogonal 3×3 supercell, the two degenerate states at T and K points of the optimum structure become nondegenerate during the molecular dynamics. For both systems, CB states at MoX_2@K and WX_2@K are represented by the deep blue and red lines. The hybridized MoX_2@T states are represented by light blue lines in between the two states.

Electron-phonon coupling induces the oscillation of the Kohn-Sham eigenenergies as shown in Figs. 2(a)–2(d). First, for both systems, the energy oscillation at 300 K is stronger than that at 100 K, because more phonons are thermally excited at 300 K. Second, comparing MoS_2/WS_2 with $MoSe_2/WSe_2$, one can find that at the same temperature the oscillation amplitudes of $MoSe_2/WSe_2$ eigenenergies are much larger. In order to understand this, we performed Fourier transform (FT) of the time evolution of selected states (MoX_2@K, MoX_2@T and WX_2@K) for the two heterostructures at 300 and 100 K, as can be seen in Figs. 2(e)–2(h). For MoS_2/WS_2, the major peaks appear around 400 cm^{-1} at both temperatures, whereas they redshift to about 230 cm^{-1} in $MoSe_2/WSe_2$. In $MoSe_2/WSe_2$, at 100 K the peak around 350 cm^{-1} has higher intensity than that at 300 K. This might be due to the different initial phonon excitations in the molecular dynamics at 100 and 300 K. By comparing the peak positions with Raman scattering experiments and first-principles calculations [51,60–62], we are able to attribute the major peaks in both systems to the A_1 vibration mode. The red shift in $MoSe_2/WSe_2$ is due to different chalcogen masses and chemical bond strengths. Based on the analysis above, we propose that A_1 is the major mode coupled with the electronic states near CBM. More photons will be excited in $MoSe_2/WSe_2$ than that of MoS_2/WSe_2 at the same temperature because A_1 is much softer in the former case, which results in the observed stronger energy oscillations.

C. Phonon-coupled charge oscillations

We then proceed to investigate the electron transfer process at the heterostructure interface with NAMD, starting with $MoSe_2/WSe_2$. The photoexcited electron was initially populated at WSe_2@K state, and the results are shown in Fig. 3. Time-dependent electron transfer between the two layers can be obtained from NAMD calculations by projecting the electron localization onto the $MoSe_2$ and WSe_2 layers,

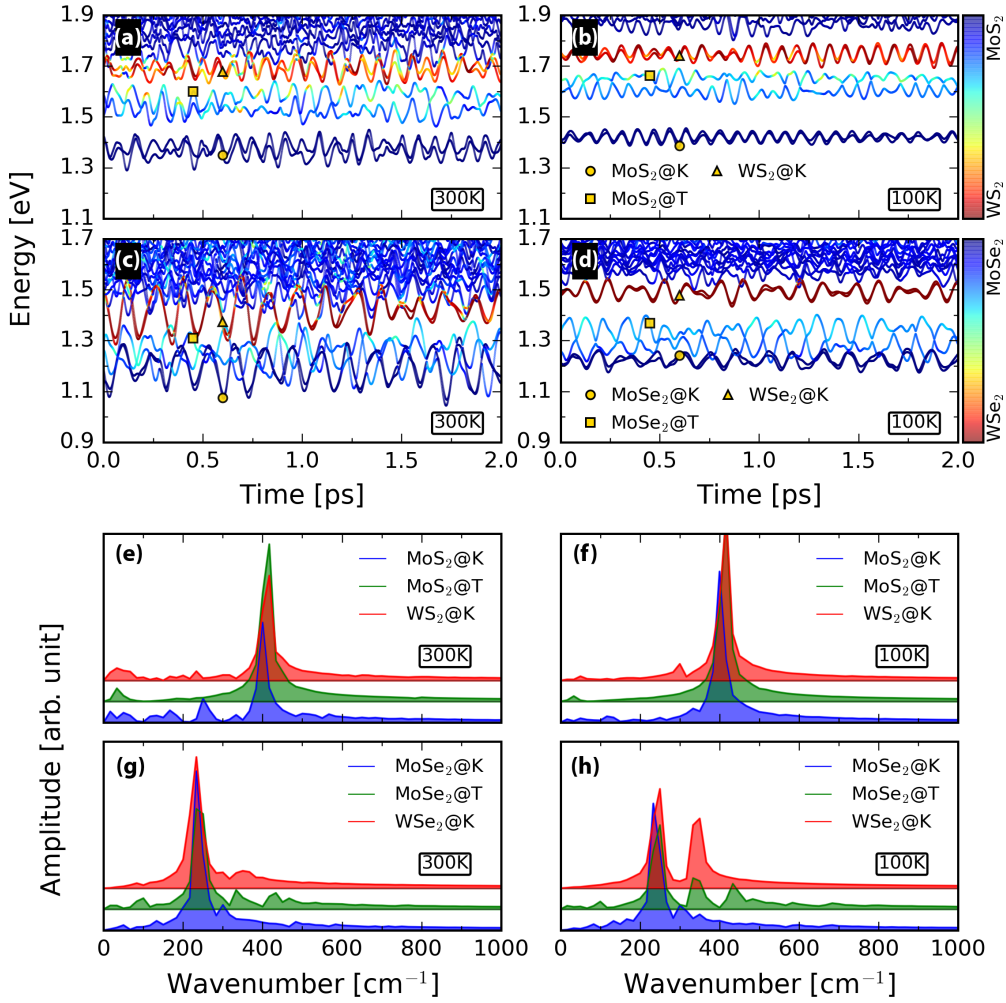

FIG. 2. Time evolutions of the energy states near CBM (a)–(d) and FT spectrum of the selected states (e)–(h) of MoX_2/WX_2(X = S, Se) heterostructures at 300 and 100 K. The energy reference in (a)–(d) is the averaged energy of WX_2@K_VB, and the color map shows the orbital localization.

as is shown in Figs. 3(a)–3(b). Moreover, time-dependent electron energy changes can also be deduced by evaluating the electron probability distribution for selected energy states from NAMD, as can be seen in Figs. 3(c)–3(d). By comparing the time-dependent localization and energy, the electron relaxation route in both real and momentum spaces can be obtained.

At 300 K, the electron localization on the WSe_2 layer [red line in Fig. 3(a)] decreases from 90% to 10%, and the electron energy [dashed line in Fig. 3(c)] drops to CBM within 1000 fs. From Fig. 3(a) it is interesting to see that the interlayer charge transfer is accompanied by a charge oscillation with a damped amplitude during the first 400 fs. We notice that the period of such an oscillation is roughly the same as that of the A_1 mode. In the momentum space, such an oscillatory charge transfer process happens between WSe_2@K and $MoSe_2$@T, followed by an intralayer charge relaxation from $MoSe_2$@T to $MoSe_2$@K. Both of these processes are intervalley charge transfer, and we propose that the phonons play a crucial role here.

In order to understand the origin of this charge oscillation and how the phonons play a role here, we decompose the charge transfer into two parts: adiabatic (AD) and nonadiabatic (NA) charge transfer. As we discuss in the methodology part, AD charge transfer is provoked by nuclear motion that causes energy states to mix. This is naturally coupled with phonons. AD charge transfer always happens when two electronic states cross each other. In contrast, NA charge transfer involves direct charge hopping or tunneling between different states. As is indicated by the green line in Fig. 3(a), the charge oscillation in the first 400 fs and the following intralayer charge relaxation are mainly contributed by AD process at 300 K, implying the important role of phonons.

To better reveal the effects of phonons, we investigate the same charge transfer process at a lower temperature of 100 K, which is expected to reduce the phonon occupation numbers. In this case, as shown in Fig. 3, the electron localization in the WSe_2 layer only decreases by 20%, while the electron energy hardly changes in 1 ps, which is much slower than that at 300 K. Additionally, there is no charge oscillation. This results in a decrease of the oscillation amplitude of energy time evolution as can be seen by comparing Figs. 2(b) and 2(d), and as a result, the crossings between the WSe_2@K and $MoSe_2$@T disappear. Therefore the AD charge transfer between them is suppressed. There is still some crossing between WSe_2@K

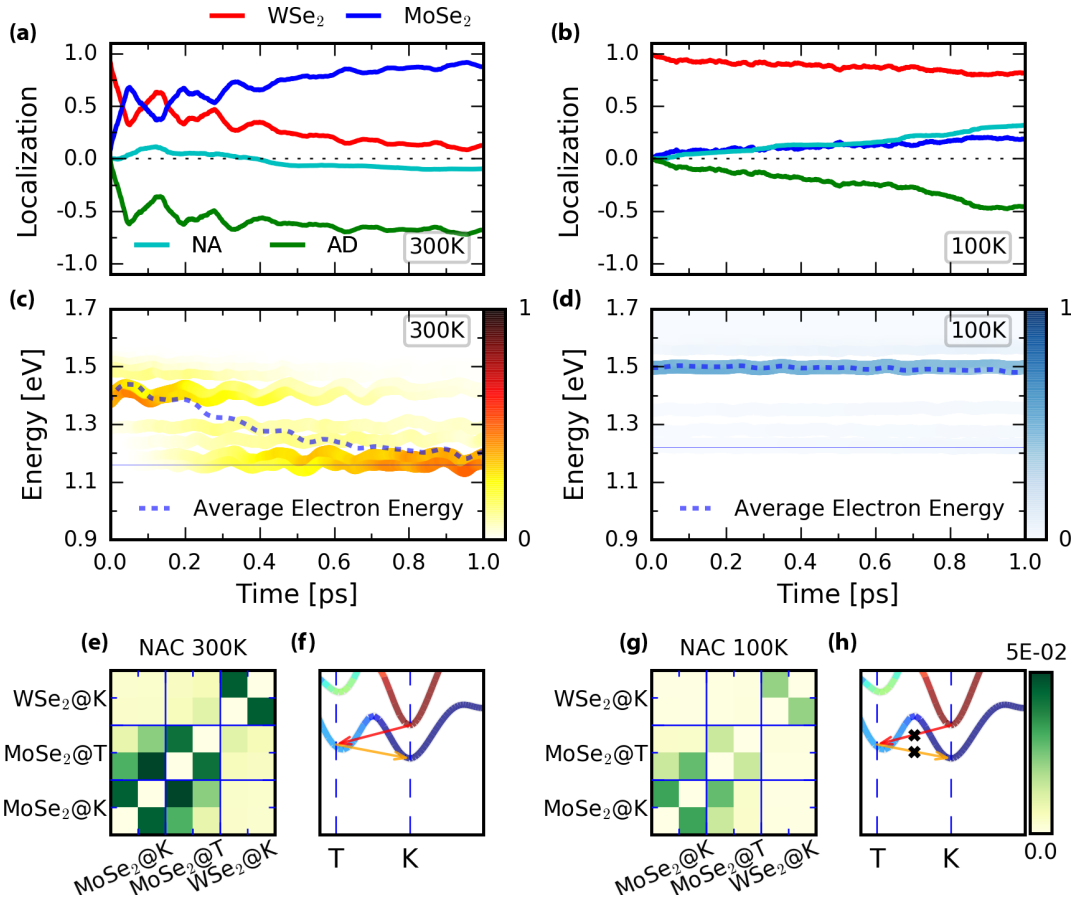

FIG. 3. Nonadiabatic molecular dynamics results of $MoSe_2/WSe_2$ at 300 and 100 K, respectively. (a)–(b) Time-dependent electron spatial localization and (c)–(d) electron energy change at 300 and 100 K. In the top part of (a)–(b) the red and blue lines shows the spatial electron localization on WSe_2 and $MoSe_2$ and in the bottom part the green and cyan lines show the AD and NA contributions of the electron transfer. The color strips in (c)–(d) indicate electron distribution among different states and the dashed lines represent the averaged electron energy. The energy reference in (c)–(d) is the averaged energy of WX_2@K_VB while the average energy of MoX_2/WX_2 CBM is indicated by the horizontal line. (e) and (g) show the averaged nonadiabatic couplings (NAC) along 2 ps NAMD trajectory at 300 and 100 K. (f) and (h) show schematics of the electron relaxation route in the momentum space.

with a $MoSe_2$ state with higher energy where the AD charge transfer can take place.

The NA charge transfer is also suppressed by the decrease in temperature. This can be understood by inspecting the nonadiabatic couplings (NACs), which determines the hopping probability between different states. The NAC is defined as:

$$d_{jk} = \varphi_j|\nabla_R|\varphi_k \cdot \dot{R} = \frac{\varphi_k|\nabla_R H|\varphi_j}{\epsilon_k - \epsilon_j}\dot{R}, \tag{3}$$

where H is the Kohn-Sham Hamiltonian, $\varphi_k, \varphi_j, \epsilon_k, \epsilon_j$ are the corresponding wave functions and eigenvalues for electronic states k and j, and $\dot{R}$ is velocity of the nuclei [63–65]. Thus, NAC elements show strong dependence on the energy difference of the interacting states, the time-dependent orbital distribution of state k and j, i.e., the e-p matrix element [66], and the nuclear velocity. All of these factors are related to e-p coupling and phonon excitation, and therefore are temperature dependent. As can be seen in Figs. 3(e) and 3(g), when the temperature decreases from 300 to 100 K, the NAC between the initial (WSe_2@K) and final states ($MoSe_2$@T and $MoSe_2$@K) becomes negligible, which explains the insufficient NA charge transfer between them. The reduction of both the AD and NA charge transfer can be understood as phonon bottleneck effects. All of these temperature-dependent results unambiguously suggest that a phonon-coupled coherent charge oscillation can be excited in $MoSe_2/WSe_2$ heterostructure through e-p coupling and that it can be suppressed through phonon reduction.

As a comparison, we perform additional NAMD calculations of the MoS_2/WS_2 heterostructure interface, where a similar electron transfer process is considered with the initial electron populated at WS_2@K. The results are significantly different from those in $MoSe_2/WSe_2$, as can be seen in Fig. 4. Here, the electron localization drops from 75% to nearly 0% within 1 ps at 300 K, and there is no charge oscillation in the electron transfer [Fig. 4(a)]. Also, the charge transfer dynamics is much less dependent on the temperature. There is no qualitative change at 100 K, where the electron localization also drops from 90% to 35% in 1 ps [Fig. 4(b)]. More analysis show that the charge transfer mainly occurs by NA mechanism at both 300 and 100 K [Figs. 4(a)–4(b)] in MoS_2/WS_2, indicating that the electron in MoS_2/WS_2 tends to relax by tunneling between donor and acceptor states rather

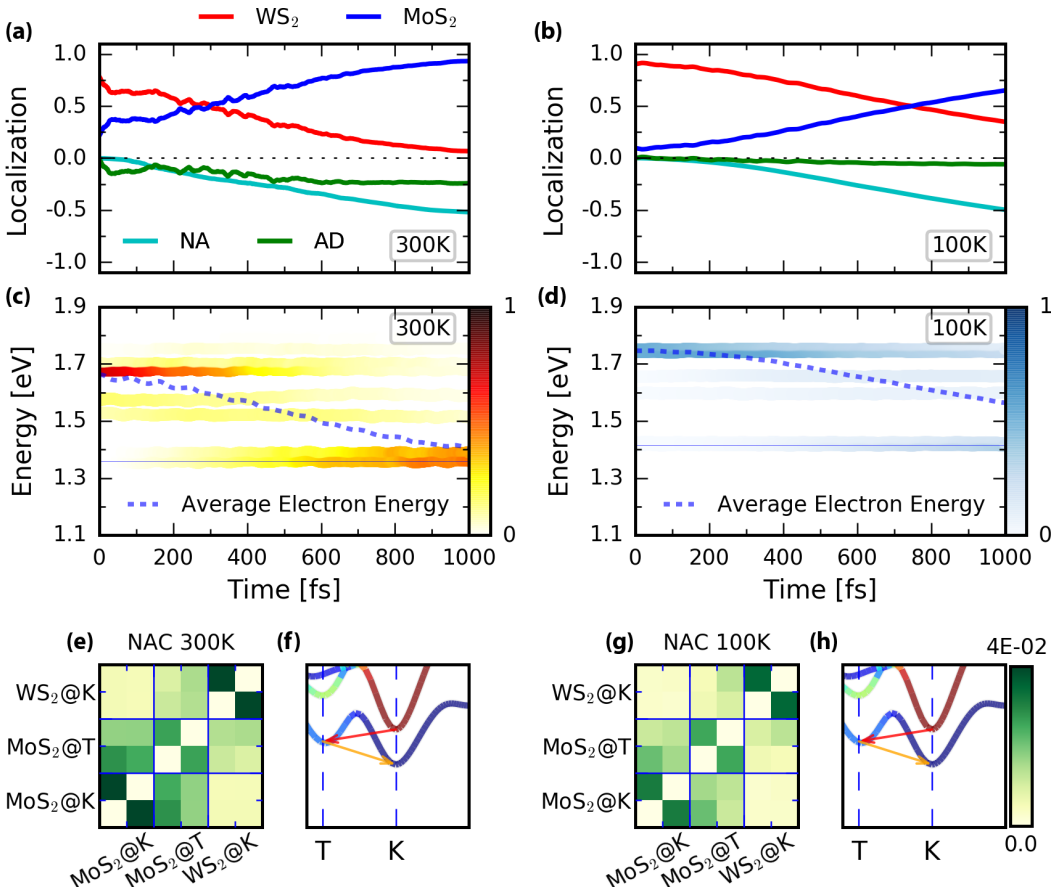

FIG. 4. Nonadiabatic molecular dynamics results of MoS_2/WS_2 at 300 and 100 K, respectively. (a)–(b) Time-dependent electron spatial localization and (c)–(d) electron energy change at 300 and 100 K. In the top part of (a)–(b) the red and blue lines shows the spatial electron localization on WS_2 and MoS_2 and in the bottom part the green and cyan lines show the AD and NA contributions of the electron transfer. The color strips in (c)–(d) indicate electron distribution among different states and the dashed lines represent the averaged electron energy. The energy reference in (c)–(d) is the averaged energy of WX_2@K_VB while the average energy of MoX_2/WX_2 CBM is indicated by the horizontal line. (e) and (g) show the averaged nonadiabatic couplings (NAC) along 2 ps NAMD trajectory at 300 and 100 K. (f) and (h) show schematics of the electron relaxation route in the momentum space.

than oscillate coherently with the phonon vibration. In the momentum space, the electron transfer proceeds by direct tunneling from WS_2@K to MoS_2@T and finally to MoS_2@K, as is shown in the schematics in Figs. 4(f) and 4(h).

The distinct behaviors between the electron transfer of MoS_2/WS_2 and $MoSe_2/WSe_2$ can be understood from two perspectives. First, the A_1 phonon mode, which is the major mode coupled with excited electrons, has a relatively low frequency in $MoSe_2/WSe_2$ (230 cm^{-1}), and therefore, sufficient phonons can be excited at 300 K. Thus through *e-p* coupling, a strong phonon-coupled coherent charge oscillation can be achieved in both energy evolution [Fig. 2(d)] and spatial localization [Fig. 3(a)]. By contrast, the frequency of A_1 mode in MoS_2/WS_2 is around 400 cm^{-1} that is higher than that in $MoSe_2/WSe_2$, which makes the phonon occupation much smaller. Therefore the phonon-coupled charge oscillation is suppressed. Second, the NAC elements between the donor (WX_2@K) and acceptor (MoX_2@T) states are larger in MoS_2/WS_2 than those in MoSe/WSe_2 at the same temperature. This is mainly because the energy difference between WX_2@K and MoX_2@T states is smaller in MoS_2/WS_2. Because of the large NAC and weak A_1 phonon excitation, charge transfer in MoS_2/WS_2 is dominated by the NA mechanism, where the charge prefers to tunnel between different states instead of coherent oscillation with the phonons. Therefore, the temperature effects in MoS_2/WS_2 are much less significant.

D. Excitonic effects estimation

So far, our NAMD calculations essentially mimic the relaxation process of free photoexcited carriers, which is not the case in experiments where the photoexcited carriers exist in the form of bound electron-hole pairs, i.e., excitons. In this paper, we use a simple method in the NAMD calculations where the excited electron energies are shifted according to the experimental value of optical absorption peaks of TMD heterostructures [51,53] to estimate the possible excitonic effects. The energy shifting technique is known as the scissor operator method and has previously been used to correct band gap errors in DFT calculations [67–69].

As schematically shown in Fig. 1(c), the intralayer exciton is first formed at K point of WX_2 with the hole locate on WX_2@K in valance band (WX_2@K_VB) and electron on CBM of WX_2. Then the electron will transfer from the WX_2 CBM to the

TABLE I. The values of interlayer band gap (E_g_inter of MoX_2/WX_2), intralayer band gap (E_g_intra for WX_2) and CBM energy offset (ΔE) obtained by DFT and absorption spectra. The deviation between experimental and DFT results is also shown.

	E_g_inter (MoS_2/WS_2)	E_g_intra (WS_2)	ΔE (MoS_2/WS_2)	E_g_inter ($MoSe_2/WSe_2$)	E_g_intra (WSe_2)	ΔE ($MoSe_2/WSe_2$)
Exp.	1.94 [51]	2.02 [51]	0.08	1.35 [53]	1.65 [53]	0.3
DFT	1.45	1.75	0.3	1.22	1.52	0.3
deviation	0.49	0.27	−0.22	0.13	0.13	0

MoX_2 CBM, forming an interlayer exciton In this process, the hole stays unchanged on WX_2@K_VB. Therefore, by choosing the energy WX_2@K_VB as a reference, the position of WX_2 CBM is determined by the WX_2 intralayer band gap (E_g_intra) and the position MoX_2 CBM is determined by the MoX_2/WX_2 interlayer band gap (E_g_inter) as we indicate in Figs. 1(a)–1(b). Taking into account the exciton effects, E_g_intra and E_g_inter should be the optical band gaps instead of the quasiparticle band gaps. The optical band gaps E_g_intra of WX_2 and E_g_inter of MoX_2/WX_2 from different previous studies based on optical absorption spectra and GW+BSE calculations are summarized in Table S1 in the Supplemental Material [48]. We use the experimental optical band gaps of WS_2 and WS_2/MoS_2 from Ref. [51] and that of WSe_2 and $WSe_2/MoSe_2$ from Ref. [53] to correct the DFT band structure. The DFT and optical band gaps by absorption spectra, as well as their deviation are summarized in Table I.

The excited electron dynamics is mostly affected by the CBM energy offset (ΔE) of WX_2 and MoX_2 [indicated in Figs. 1(a)–1(b)], which is determined from the E_g_intra of WX_2 and E_g_inter of MoX_2/WX_2 as $\Delta E = E_g$_intra$-E_g$_inter. Using the experimental optical band gaps,

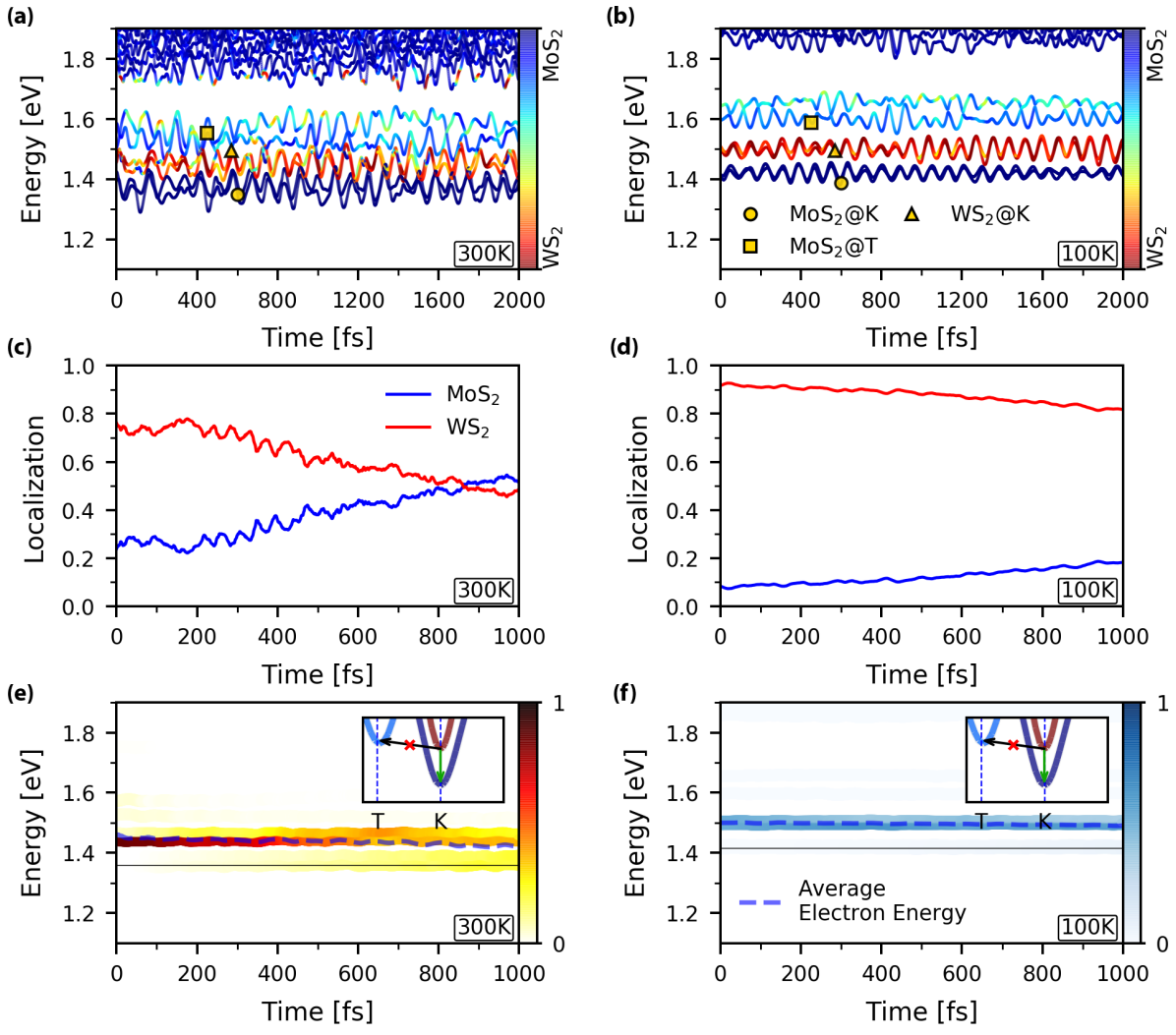

FIG. 5. NAMD results after applying scissor operator for exciton effects. (a)–(b) Time evolutions of the energy states near CBM at 100 and 300 K. (c)–(d) Time-dependent electron spatial localization and (e)–(f) electron energy change at 100 and 300 K. The color strips in (e)–(f) indicate electron distribution among different states and the dashed lines represent the averaged electron energy. The energy reference in (c)–(d) is the averaged energy of WX_2@K_VB while the average energy of CBM is indicated by the horizontal line.

ΔE is calculated to be 0.08 and 0.3 eV for MoS_2/WS_2 and $MoSe_2/WSe_2$ as shown in Table I. In comparison, the ΔE obtained by DFT is 0.3 eV for both of them. Therefore, one can see that the energy shift due to exciton binding decrease the CBM energy offset of MoS_2/WS_2 significantly, while as for $MoSe_2/WSe_2$, it has little effect. As shown in the insets of Figs. 5(e)–5(f), due to the significant decrease of ΔE in MoS_2/WS_2, after the band shifting by the scissor operator, the WS_2@K is moved below the MoS_2@T state. Since the excited electron has very little probability to transfer to a state with higher energy, the intervalley charge transfer route from WS_2@K to MoS_2@T is blocked. The excited electron can only decay from WS_2@K to MoS_2@K directly. Thus, the excited electrons at WS_2@K decay much slower both at 100 and 300 K as shown in Fig. 5.

E. Discussion

Taking MoS_2/WS_2 and $MoSe_2/WSe_2$ as prototype systems with good contrast, we found that phonon excitation is one crucial factor affecting the interlayer charge transfer, which can be tuned using different experimental techniques. The phonon excitation is strongly affected by the phonon frequency, which is determined by the chemical bonding strength. It can be tuned by changing the elements (for example S versus Se as we show in this report) or by applying external stress. For example, in 2D graphene and MoS_2, the phonons have been found to soften by application of a tensile stress [70,71]. Further, recently the phonon pumping techniques using infrared light have been used to excite resonant lattice phonons and phonon-dressed electronic states [72–76]. With such a technique, we can expect that A_1 mode and the coherent charge oscillation in $MoSe_2/WSe_2$ can be selectively excited.

In this paper, we use the scissor operator method to estimate the exciton effects on the electron transfer at MoS_2/WS_2 and $MoSe_2/WSe_2$ interface. It is needed to be clarified that in this method only the shift of energy is considered. The wave functions used to calculate the NA coupling is still on the DFT level. Based on this simple estimation, the electron transfer dynamics of MoS_2/WS_2 is possible to be significantly affected. More accurate treatments of the exciton effects are essential for the future study.

IV. SUMMARY

To summarize, using *ab initio* NAMD, taking MoS_2/WS_2 and $MoSe_2/WSe_2$, which have similar band structures yet different phonon frequencies as prototype systems, we study the *e-p* coupling effects on the photoexcited interlayer electron transfer. We found that for both systems, the intralayer optical A_1 mode couples mostly with the electron dynamics. For $MoSe_2/WSe_2$, which has a lower A_1 phonon frequency, a phonon-coupled charge oscillation can be excited at room temperature with sufficient phonon excitation. Such a charge oscillation is difficult to excite in MoS_2/WS_2 since the A_1 phonon frequency is higher the phonon excitation is more difficult. Such phonon excitation can be tuned by different experimental techniques and therefore the phonon-coupled charge oscillation is possible to be controlled. The atomic level picture on how the phonons affect the interlayer charge transfer dynamics provides specific new insights for the fundamental understanding of ultrafast dynamics at vdW hetero-interfaces, and the design of novel quasi-2D devices for optoelectronic and solar energy conversion applications.

ACKNOWLEDGMENTS

This work is supported by NSFC (Grants No. 11620101003, No. 11704363, and No. 21421063), by National Key Basic Research Program of China (Grants No. 2016YFA0200604 and No. 2017YFA0204904), the Fundamental Research Funds for the Central Universities WK3510000005. W.A.S. acknowledges a startup fund from the University of Pittsburgh. O.V.P. acknowledges financial support of the US National Science Foundation, Grant No. CHE-1565704. Calculations were performed at Environmental Molecular Sciences Laboratory at the PNNL, a user facility sponsored by the DOE Office of Biological and Environmental Research and USTC supercomputing center. We thank Z. Zhang and J. Yang for valuable discussions.

[1] K. F. Mak, C. Lee, J. Hone, J. Shan, and T. F. Heinz, Phys. Rev. Lett. **105**, 136805 (2010).
[2] K. F. Mak, K. He, J. Shan, and T. F. Heinz, Nature Nanotechnol. **7**, 494 (2012).
[3] G. Eda, H. Yamaguchi, D. Voiry, T. Fujita, M. Chen, and M. Chhowalla, Nano Lett. **11**, 5111 (2011).
[4] T. Cheiwchanchamnangij and W. R. L. Lambrecht, Phys. Rev. B **85**, 205302 (2012).
[5] A. Ramasubramaniam, Phys. Rev. B **86**, 115409 (2012).
[6] M. Bernardi, M. Palummo, and J. C. Grossman, Nano Lett. **13**, 3664 (2013).
[7] P. Rivera, K. L. Seyler, H. Yu, J. R. Schaibley, J. Yan, D. G. Mandrus, W. Yao, and X. Xu, Science **351**, 688 (2016).
[8] X. Wang and F. Xia, Nature Mater. **14**, 264 (2015).
[9] X. Hong *et al.*, Nature Nanotechnol. **9**, 682 (2014).
[10] L. Britnell *et al.*, Science **340**, 1311 (2013).
[11] F. Withers *et al.*, Nature Mater. **14**, 301 (2015).
[12] W. J. Yu, Y. Liu, H. Zhou, A. Yin, Z. Li, Y. Huang, and X. Duan, Nature Nanotechnol. **8**, 952 (2013).
[13] Q. H. Wang, K. Kalantar-Zadeh, A. Kis, J. N. Coleman, and M. S. Strano, Nature Nanotechnol. **7**, 699 (2012).
[14] J. Feng, X. Qian, C.-W. Huang, and J. Li, Nature Photon. **6**, 866 (2012).
[15] J. Kang, S. Tongay, J. Zhou, J. Li, and J. Wu, Appl. Phys. Lett. **102**, 012111 (2013).
[16] C. Gong, H. Zhang, W. Wang, L. Colombo, R. M. Wallace, and K. Cho, Appl. Phys. Lett. **103**, 053513 (2013).
[17] H.-P. Komsa and A. V. Krasheninnikov, Phys. Rev. B **88**, 085318 (2013).
[18] H. Terrones, F. López-Urías, and M. Terrones, Sci. Rep. **3**, 1549 (2013).
[19] K. Kośmider and J. Fernández-Rossier, Phys. Rev. B **87**, 075451 (2013).

[20] D. Y. Qiu, F. H. da Jornada, and S. G. Louie, Phys. Rev. Lett. **111**, 216805 (2013).
[21] A. M. Jones *et al.*, Nature Nanotechnol. **8**, 634 (2013).
[22] M. M. Ugeda *et al.*, Nature Mater. **13**, 1091 (2014).
[23] F. Ceballos, M. Z. Bellus, H.-Y. Chiu, and H. Zhao, ACS Nano **8**, 12717 (2014).
[24] X. Zhu, N. R. Monahan, Z. Gong, H. Zhu, K. W. Williams, and C. A. Nelson, J. Am. Chem. Soc. **137**, 8313 (2015).
[25] C.-H. Lee *et al.*, Nature Nanotechnol. **9**, 676 (2014).
[26] H. Wang, J. Bang, Y. Sun, L. Liang, D. West, V. Meunier, and S. Zhang, Nature Commun. **7**, 11504 (2016).
[27] R. Long and O. V. Prezhdo, Nano Lett. **16**, 1996 (2016).
[28] Q. Zheng, W. A. Saidi, Y. Xie, Z. Lan, O. V. Prezhdo, H. Petek, and J. Zhao, Nano Lett. **17**, 6435 (2017).
[29] Z. Ji *et al.*, ACS Nano **11**, 12020 (2017).
[30] G. Moody, J. Schaibley, and X. Xu, J. Opt. Soc. Am. B **33**, C39 (2016).
[31] W. R. Duncan and O. V. Prezhdo, Annu. Rev. Phys. Chem. **58**, 143 (2007).
[32] C. F. Craig, W. R. Duncan, and O. V. Prezhdo, Phys. Rev. Lett. **95**, 163001 (2005).
[33] L. Wang, R. Long, and O. V. Prezhdo, Annu. Rev. Phys. Chem. **66**, 549 (2015).
[34] O. V. Prezhdo, W. R. Duncan, and V. V. Prezhdo, Prog. Surf. Sci. **84**, 30 (2009).
[35] O. V. Prezhdo, W. R. Duncan, and V. V. Prezhdo, Acc. Chem. Res. **41**, 339 (2008).
[36] W. Chu, W. A. Saidi, Q. Zheng, Y. Xie, Z. Lan, O. V. Prezhdo, H. Petek, and J. Zhao, J. Am. Chem. Soc. **138**, 13740 (2016).
[37] C. Zhao, Q. Zheng, J. Wu, and J. Zhao, Phys. Rev. B **96**, 134308 (2017).
[38] http://staff.ustc.edu.cn/∼zhaojin/code.html.
[39] G. Kresse and J. Hafner, Phys. Rev. B **47**, 558 (1993).
[40] G. Kresse and J. Hafner, Phys. Rev. B **48**, 13115 (1993).
[41] G. Kresse and J. Hafner, Phys. Rev. B **49**, 14251 (1994).
[42] G. Kresse and J. Furthmüller, Phys. Rev. B **54**, 11169 (1996).
[43] A. V. Akimov and O. V. Prezhdo, J. Chem. Theo. Comput. **9**, 4959 (2013).
[44] A. V. Akimov and O. V. Prezhdo, J. Chem. Theo. Comput. **10**, 789 (2014).
[45] G. Kresse and D. Joubert, Phys. Rev. B **59**, 1758 (1999).
[46] J. P. Perdew, K. Burke, and M. Ernzerhof, Phys. Rev. Lett. **77**, 3865 (1996).
[47] S. Grimme, J. Comput. Chem. **27**, 1787 (2006).
[48] See Supplemental Material at http://link.aps.org/supplemental/10.1103/PhysRevB.97.205417 for more details of the calculation method, the selection of supercell and k points, the discussion of spin orbit coupling effects, stacking effects, k-point grid effects, and different-functional effects.
[49] P. E. Blöchl, Phys. Rev. B **50**, 17953 (1994).
[50] J. C. Tully, J. Chem. Phys. **93**, 1061 (1990).
[51] J. Zhang *et al.*, Adv. Mater. **28**, 1950 (2016).
[52] B. Zhu, X. Chen, and X. Cui, Sci. Rep. **5**, 9218 (2015).
[53] P. Rivera *et al.*, Nature Commun. **6**, 6242 (2015).
[54] A. Chernikov, T. C. Berkelbach, H. M. Hill, A. Rigosi, Y. Li, O. B. Aslan, D. R. Reichman, M. S. Hybertsen, and T. F. Heinz, Phys. Rev. Lett. **113**, 076802 (2014).
[55] Z. Ye, T. Cao, K. O'Brien, H. Zhu, X. Yin, Y. Wang, S. G. Louie, and X. Zhang, Nature (London) **513**, 214 (2014).
[56] H. Yu, Y. Wang, Q. Tong, X. Xu, and W. Yao, Phys. Rev. Lett. **115**, 187002 (2015).
[57] H. Heo *et al.*, Nature Commun. **6**, 7372 (2015).
[58] P. K. Nayak *et al.*, ACS Nano **11**, 4041 (2017).
[59] P. Nagler *et al.*, Nature Commun. **8**, 1551 (2017).
[60] Y. Gong *et al.*, Nat. Mater. **13**, 1135 (2014).
[61] S. V. Bhatt, M. P. Deshpande, V. Sathe, R. Rao, and S. H. Chaki, J. Raman Spec. **45**, 971 (2014).
[62] B. Amin, T. P. Kaloni, G. Schreckenbach, and M. S. Freund, Appl. Phys. Lett. **108**, 063105 (2016).
[63] I. Tavernelli, B. F. E. Curchod, and U. Rothlisberger, J. Chem. Phys. **131**, 196101 (2009).
[64] C. Hu, H. Hirai, and O. Sugino, J. Chem. Phys. **128**, 154111 (2008).
[65] K. G. Reeves, A. Schleife, A. A. Correa, and Y. Kanai, Nano Lett. **15**, 6429 (2015).
[66] G. Grimvall, *The Electron-Phonon Interaction in Metals*, Selected Topics in Solid State Physics (North-Holland, New York, 1981)
[67] R. W. Godby, M. Schlüter, and L. J. Sham, Phys. Rev. B **37**, 10159 (1988).
[68] F. Gygi and A. Baldereschi, Phys. Rev. Lett. **62**, 2160 (1989).
[69] K. A. Johnson and N. W. Ashcroft, Phys. Rev. B **58**, 15548 (1998).
[70] F. Liu, P. Ming, and J. Li, Phys. Rev. B **76**, 064120 (2007).
[71] T. Li, Phys. Rev. B **85**, 235407 (2012).
[72] W. Hu *et al.*, Nature Mater. **13**, 705 (2014).
[73] M. Mitrano *et al.*, Nature (London) **530**, 461 (2016).
[74] Y. H. Wang, H. Steinberg, P. Jarillo-Herrero, and N. Gedik, Science **342**, 453 (2013).
[75] I. Gierz *et al.*, Phys. Rev. Lett. **115**, 086803 (2015).
[76] E. Pomarico *et al.*, Phys. Rev. B **95**, 024304 (2017).